Supplementary Information for

"High concentration of ultrafine particles in the Amazon free troposphere produced by organic new particle formation"

This PDF file includes:

Sections 1 to 8

Figures S1 to S16

Table S1 to S3

1. Description of the radical 2D-VBS framework and determination of its parameterization

In the radical 2D-VBS framework (1), organic species are lumped into the C* and O:C space with C* ranging from 10^{-10} to 10^{6} μg m^{-3}, separated by powers of 10 (i.e., 17 bins in total), and O:C ranging from 0 to 1.3, separated by 0.1 (i.e., 14 bins in total). The reactions begin with oxidation of monoterpene with O_3, OH, and NO_3, producing peroxy radicals (RO_2). The peroxy radicals will undergo two types of reactions: autoxidation or radical termination. Autoxidation generates a more oxidized peroxy radical that will undergo further autoxidation or termination. Since only some peroxy radicals may have rapid autoxidation pathways, we distinguish in the model two types of peroxy radicals: one has the potential for autoxidation and the other does not. The radical termination proceeds via unimolecular termination or reactions with HO_2, NO, or another peroxy radical. The peroxy radical cross-reactions can produce dimers (ROOR), the fraction of which in all cross-reaction products is assumed to depend on the volatility of the two reacting peroxy radicals. The non-dimer cross-reaction products as well as the termination products via unimolecular termination or reaction with NO will undergo either functionalization or fragmentation with a branching ratio (br, defined as the fraction of fragmentation among the

two competing pathways). We map the stable molecules generated from each peroxy radical termination pathway to a distribution of species in the 2D-VBS space through kernels, which allow us to represent the wide variety of both the peroxy radicals and the stabilization reactions (1). Kernels, which were first described for the 2D-VBS in Donahue et al. (2) (e.g. Fig. S1), define the rule to map a reactant of any given volatility and O:C (termination products of peroxy radical in the case of the radical 2D-VBS) to a distribution of reaction products in the 2D-VBS framework. They are established based on experimental data and a-priori consideration of organic oxidation methods as well as functional-group contributions to volatility. The kernels used in this work are summarized in Table S3–S6 of Schervish and Donahue (1).

We simulate a series of laboratory experiments with the radical 2D-VBS, compare modeled HOM yields and SOA concentrations with measurements, and optimize key 2D-VBS parameters to achieve a good model-measurement agreement. Before going into details, we would like to mention that, purely in terms of the number of parameters, the radical 2D-VBS is more tunable than many other modeling approaches (though it is an enormous simplification of actual organic oxidation mechanisms). This is why the long-standing methodology associated with the VBS has been to employ a disciplined approach, reducing the degrees of freedom via the oxidation kernels described above. Because of this, the effective number of degrees of freedom is reduced to a handful of branching ratios between different termination reactions. This approach substantially reduces the tuneability but still reasonably represents the variety of both the peroxy radicals and the stabilization reactions. For example, in the simulations of laboratory experiments we only perturb three key parameters within a theoretically reasonable a-priori range while keeping other parameters (e.g., reaction rate coefficients) at the default values derived from kinetic literature (1). The three key parameters are: the fraction of first-generation peroxy radicals that can potentially

autoxidize in all those formed via 1) the α-pinene + O_3 reaction (f_{O3}) and 2) the α-pinene + OH reaction (f_{OH}), and finally, 3) br. Among all 2D-VBS parameters, these three parameters are comparatively uncertain and significantly influence simulated HOM and SOA concentrations; therefore, we opt to optimize their values through simulation and evaluation against laboratory experiments. This in reality is hardly, if at all, more tunable than a scheme that arbitrarily selects a fraction of oxidation products from a few precursors to condense to or nucleate particles (a common approach in global models).

1.1 Simulation of HOM yields and comparison with experimental data

We simulate a number of laboratory experiments, which measured the yields of HOMs from α-pinene + O_3 (3-6) and α-pinene + OH (3-5, 7). Table S2 and S3 summarize the experimental conditions for these experiments and the corresponding conditions we use in the 2D-VBS simulations. The O_3 concentrations used in these experiments (12–86 ppb) are similar to observations in the pristine conditions of the Amazon boundary layer (8–17 ppb) (8-10). The OH and α-pinene concentrations in the experiments cover a wide range, i.e., from 4×10^4 to 4×10^8 mole cm^{-3} for OH and from ~0.05 to 160 ppb for α-pinene. These concentration ranges include observed concentrations in relatively pristine conditions of the Amazon boundary layer, i.e., 2–5×10^5 mole cm^{-3} for OH (11) and 0.14–0.9 ppb for monoterpenes (12-14). In the 2D-VBS simulations, we tried to exactly reproduce the experimental conditions whenever possible. Some studies (e.g., Sarnela et al. (6)) performed only a handful of experiments and listed the conditions for all experiments, thus we simulated each and every experiment based on the exact conditions. Other studies (3-5, 7), however, conducted a large number of experiments without providing the conditions or HOM yields of each individual experiment; in this case, we conducted several typical

model runs with α-pinene and/or oxidant concentrations representing relatively high and low levels within the experimental range (see Table S2 and S3).

As mentioned above, we adjust the values of f_{O3}, f_{OH}, and br in our simulations and keep the other parameters at their default values (1). Note that f_{O3} and f_{OH} represent the fractions of *first-generation* peroxy radicals that can potentially autoxidize. These "autoxidizable" peroxy radicals are allowed to undergo up to three generations of autoxidation in the model. The fraction of peroxy radicals actually autoxidized differs between simulations, depending on the relative rates of autoxidation and bimolecular reactions.

For a fair comparison between simulated and measured HOM yields, we adopt a widely accepted HOM definition, where HOMs are organic compounds containing at least six oxygen atoms formed through autoxidation and subsequent termination processes (15). In the 2D-VBS context, autoxidized monomers with O:C ≥ 0.6 and autoxidized dimers with O:C ≥ 0.3 are regarded as HOMs. Figures S9 and S10 compare 2D-VBS simulated HOM molar yields with measurements from laboratory experiments involving α-pinene + O_3 and α-pinene + OH reactions, respectively. While all three parameters perturbed affect HOM molar yields, f_{O3} and f_{OH} are found to have the largest impact on HOM yields from α-pinene + O_3 and α-pinene + OH, respectively. Therefore, Figures S9 and S10 only show the simulation results when perturbing the most sensitive parameter, with the other two parameters set to the final values used in our 3-D simulations. To determine the optimal parameters, we estimate the mean bias (MB) of HOM yield:

$$MB = \frac{1}{N}\sum_{n=1}^{N}\left(\frac{1}{M(n)}\sum_{m=1}^{M(n)}\left(Y_{m,n}^{sim} - Y_{m,n}^{expt}\right)\right)$$

where $Y_{m,n}^{sim}$ is the simulated HOM yield in the mth run for the nth experimental study and $Y_{m,n}^{expt}$ is the corresponding measured value; $M(n)$ is the number of runs for the nth study; N is the number of studies considered in this work (as summarized in Table S2 and S3).

Figure S9 shows that the simulated HOM yield from α-pinene + O_3 increases roughly linearly with f_{O3}. The minimum MB is achieved at $f_{O3} = 0.25$, which gives a MB = −0.0012. At this f_{O3}, the 2D-VBS simulated HOM yields agree fairly well with experimental data in almost all studies. Similarly, for HOM yield from α-pinene + OH, f_{OH} = 0.10 gives a minimum MB of -2.1×10^{-5} (Fig. S10). Compared with the α-pinene + O_3 reaction, however, the measured HOM yields from α-pinene + OH reaction show a relatively large variability, partly because OH-initiated HOMs are highly sensitive to the choice of detection technique (7). Hence, the 2D-VBS with the optimal f_{OH} overestimates the HOM yield from Jokinen et al. (5) while underestimating that from Berndt et al. (7).

1.2 Simulation of SOA concentrations and comparison with experimental data

In addition to HOMs, we also simulate a number of laboratory experiments that measured SOA production from α-pinene. These experiments involve reactions of α-pinene with O_3 (16, 17) and OH (18), under both high-NO_x (17, 18) and low-NO_x (16-18) conditions. We use different experiments to constrain HOM and SOA simulation results because previous studies seldom reported HOM and SOA yields simultaneously. To better represent the atmospheric conditions over the Amazon, we select experiments with relatively low aerosol mass concentrations. The experimental conditions (which are also the conditions for 2D-VBS simulations) have been summarized in Table 1 of Shilling et al. (16), Table 1 of Presto et al. (17), and Table 2 of Ng et al. (18). The measured and simulated SOA concentrations for all experiments are illustrated in Fig. S11. These experiments span an SOA concentration range of ~0.1 to 200 μg m^{-3}. Observational

studies (9, 14, 19) in the Amazon boundary layer showed OA concentrations of 1.0–9.0 μg m^{-3} averaged across various conditions in the wet and dry seasons and 0.2–0.6 μg m^{-3} under relatively pristine conditions; in the upper troposphere, Andreae et al. (19) reported an OA concentration of 1.6 μg m^{-3} (normalized to standard temperature and pressure, STP) in the dry season. Therefore, the OA concentration range in the experiments covers ambient concentrations over the Amazon. As with the HOM yields, we adjust f_{O3}, f_{OH}, and br in the simulations, but only show in Fig. S11 the simulation results when br is adjusted while the other two parameters are held fixed at the final values used in our 3-D simulations, since the simulated SOA concentration is most sensitive to br. Given the large range of SOA concentrations, we use the mean normalized bias (MNB) of SOA concentrations (cf. MB for HOM yields) to determine the optimal parameters.

$$MNB = \frac{1}{N}\sum_{n=1}^{N}\left(\frac{1}{M(n)}\sum_{m=1}^{M(n)}\left(SOA_{m,n}^{sim} - SOA_{m,n}^{expt}\right)/SOA_{m,n}^{expt}\right)$$

where $SOA_{m,n}^{sim}$ is the simulated SOA concentration in the m^{th} run for the n^{th} experimental study and $SOA_{m,n}^{expt}$ is the corresponding measured value; $M(n)$ is the number of runs for the n^{th} study; N is the number of studies considered in this work.

Figure S11 shows that the simulated SOA concentrations decrease when br increases from (a) to (f). The minimum MNB is achieved at $br = (O{:}C)^{1/2}$, which gives a MNB = 0.7%. At this br, the 2D-VBS simulated SOA concentrations agree reasonably well with experimental data in most studies.

To examine the influence on our atmospheric simulations of the parameter optimization to fit SOA experiments, we conducted a sensitivity analysis using the default 2D-VBS parameters in Schervish and Donahue (1), where fragmentation is not assumed to occur (i.e., functionalization is 100%). The results are illustrated in Fig. S16. Compared with the case without fragmentation,

the base case used in this study predicts lower OA concentrations and is closer to observations most of the time except for a few brief periods (e.g., 14:31–14:38 UTC). Nevertheless, the difference between these two cases is not large because the change of parameters only affects monoterpene SOA, while the SOA derived from other precursors are simulated with a 1D-VBS (20) in both cases. The present study focuses on the simulation of NPF. Because of this we only optimize the 2D-VBS parameters for monoterpenes, which are linked to NPF in the model. If we optimized the parameters for other precursors against laboratory experiments as well, we would expect a larger difference between the simulation results using optimized and default parameters.

1.3 Temperature dependence of HOM yields

Compared with the above evaluations near room temperature (278–298 K), it is more challenging to evaluate simulated temperature dependence of HOM yields. While it has been well recognized that the autoxidation rate and hence the HOM yield is strongly temperature dependent, there are some challenges in accurately measuring the HOM yield at low temperature, partly because the condensation loss of HOMs as well as the losses to chamber wall or sampling lines are much enhanced due to substantially reduced volatility at low temperature. Stolzenburg et al. (21) measured the yields and gas-phase spectra of HOMs from α-pinene + O_3 at 298 K, 278 K, and 248 K in the CLOUD (Cosmics Leaving Outdoor Droplets) chamber, and found that the calculated particle growth rates and composition based on these HOM vapor measurements are consistent with both measured growth rates and particle-phase composition. Therefore, we consider their measurements to be the most robustly constrained values available regarding the temperature dependence of HOM yields. The results showed that the HOM yield decreases by a factor of ~20 when temperature decreases from 298 K to 248 K. Our 2D-VBS simulations at their experimental conditions (0.6 ppb α-pinene, 40 ppb O_3, dark) show that the HOM yield decreases

by a factor of 25 from 298 K to 248 K, quite similar to the results of Stolzenburg et al. (21). A more systematic evaluation of the temperature-dependence of HOM yield will be warranted when more well-constrained experimental data become available.

1.4 Consideration about high-NO_x vs. low-NO_x conditions

While the HOM yield measurements employed in this study were mostly conducted under low-NO_x conditions (such measurements have rarely been conducted under high-NO_x conditions), the SOA concentration measurements cover both high-NO_x and low-NO_x conditions. We include experiments spanning a wide range of environmental conditions to enable a broad applicability of our model. Our model considers some of the NO_x dependency by explicitly treating the competition between different reaction pathways of peroxy radicals (e.g., RO_2 + NO vs. autoxidation, RO_2 + HO_2, and RO_2 + RO_2). However, we did not consider the NO_x dependency of the subsequent stabilization reactions of peroxy radical termination products because that is not the focus of this study. Figure S11d shows that, with the optimal parameters, the simulated SOA concentrations agree fairly well with measurements under both high-NO_x and low-NO_x conditions, though some discrepancies exist. Nevertheless, considering that this study focuses on the pristine areas of the Amazon where the low-NO_x conditions prevail, we also conduct a sensitivity simulation in which the 2D-VBS parameters are determined only based on evaluation against low-NO_x experiments. In this case, the branching ratio that agrees best with experimental data is $br = 0.9 \times (O{:}C)$ (f_{O3} and f_{OH} are unchanged). Figure S15 compares simulated OA concentrations in the base case and the sensitivity case ("low-NO_x only") with G-1 observations on March 7. This parameter change from our base case has only a slight effect on the simulated OA concentrations, because 1) the adjusted parameters are not too far from the original ones, and 2) they only affect

SOA formed from monoterpenes. The effect on NPF is also small given the relatively small influence of br on HOM yield.

2. Configuration of the updated WRF-Chem model for application to the Amazon

We apply our updated WRF-Chem model to a domain covering the central Amazon basin with a grid spacing of 10 km (Fig. 1). The vertical resolution includes 45 layers from the surface to 50 hPa with more closely spaced layers at lower altitudes. The gas chemistry and equilibrium gas-particle partitioning of monoterpene and its oxidation products are modeled using the radical 2D-VBS. Other gas and aerosol chemistry is simulated using the SAPRC99 gas chemistry scheme (22) coupled with the MOSAIC (Model for Simulating Aerosol Interaction and Chemistry) aerosol module (23) and a one-dimensional VBS (20) for SOA modeling. The aqueous-phase chemistry is based on the Carnegie Mellon University (CMU) scheme of Fahey and Pandis (24).

The meteorological initial and boundary conditions are generated from the National Centers for Environmental Prediction (NCEP) Climate Forecast System Version 2 reanalysis data (CFSv2) at a 0.5º×0.5º and 6-h resolution. The chemical initial and boundary conditions are provided by a quasi-global WRF-Chem simulation in 2014 (25, 26). A 5-day spin-up period is used to minimize the influence of initial conditions on simulation results. The version of WRF-Chem used for the quasi-global simulations employed the same treatment of aerosol transport, dry deposition, and wet removal as our modified version. However, the quasi-global version used 8 aerosol size bins (cf. 20 bins in our modified version) and did not consider the formation of ultra- and extremely low volatility organic compounds (ULVOC and ELVOC) nor their contributions to NPF. Note that almost all ULVOC and ELVOC are produced locally and instantaneously, rather than transported from elsewhere or accumulated over time, because they have a very short gas-phase lifetime in the atmosphere due to their extremely low volatilities and consequent condensational loss.

Nevertheless, the simplified treatment in the quasi-global simulation may to some extent underestimate the loading of pre-existing aerosols advected into the simulation domain, which may subsequently affect the condensation sink of ULVOC/ELVOC that drive organic NPF. To examine the potential effect of the boundary conditions, we divide the simulation domain into 9 (3×3) equal blocks. Since the prevailing winds were northeasterly during both the wet-season and dry-season simulation periods, aerosols were predominantly transported from northeast to southwest. Therefore, we can use the lower left block of the domain to test potential sensitivity to boundary conditions. The other 8 blocks, in which the aerosol fields are simulated by our modified version of WRF-Chem, effectively constitute the outer domain for this block. In this lower-left block, we find that, during the wet-season and dry-season periods, ultrafine particles < 50 nm account for 90% and 73% of the total aerosol surface area in the upper troposphere above 13 km, respectively. These ultrafine particles are predominantly produced by local NPF and not transported from other regions (the other 8 blocks in this case), because transported aerosols have usually grown to larger sizes. In other words, the upper-tropospheric aerosol surface area is likely dominated by locally formed ultrafine particles. For this reason, we conclude that the simplified aerosol treatment in the quasi-global simulations should only moderately affect the pre-existing aerosol surface area and NPF rates in the simulation domain, and so should not affect the major conclusions of this study.

The physical options used include the Community Land Model Version 4 (CLM4) (27), the Yonsei University (YSU) PBL scheme (28), the Grell-Freitas cumulus scheme (29), the Morrison double-moment scheme for cloud microphysics (30), and the Rapid and accurate Radiative Transfer Model for GCM (RRTMG) shortwave and longwave radiation scheme (31). For aerosol-cloud interactions, aerosols are activated based on the parameterization of Abdul-Razzak and Ghan (32), which is subsequently coupled with the Morrison cloud microphysics scheme. The grid-scale

wet removal of chemical species is simulated based on Easter et al. (33). The approach to simulate subgrid convective transport and wet removal of chemical species was developed by Grell and Devenyi (34) and described in more details by Grell and Freitas (29). Both the grid-scale and subgrid schemes treat the wet removal of aerosols and some inorganic gases (such as SO_2, H_2O_2, CH_3O_2H, O_3, H_2SO_4, and methanesulfonic acid) without considering the wet removal of organic gases. Theoretically, deep convective clouds that transport precursors of ULVOC and ELVOC to the upper troposphere are efficient removers of soluble species. Nevertheless, primary biogenic volatile organic compounds (VOCs) and their less oxidized reaction products usually have low solubility and are thus not susceptible to wet removal. Highly oxidized reaction products are more soluble, but they will be rapidly removed by condensation due to their low volatilities even without considering wet removal. In fact, as we mentioned above, almost all upper-tropospheric ULVOC and ELVOC are produced locally rather than transported from the lower troposphere in our model. Therefore, neglecting wet removal of organic gases should have limited impact on simulated ULVOC and ELVOC concentrations in the upper troposphere. Even so, an improved treatment of wet removal of organic gases with a sophisticated parameterization of solubility will enable a more accurate simulation of upper-tropospheric ULVOC and ELVOC concentrations, which warrants future model development and further studies.

We employ the Amazon anthropogenic emission inventory used by Shrivastava et al. (10), which combines several emission inventories from different sources to obtain reasonable estimates of trace gases and aerosol emissions. The biogenic emissions are calculated online using the Model of Emissions of Gases and Aerosols from Nature (MEGAN v2.1) (35) that has been recently coupled within the land surface scheme CLM4 in WRF-Chem (36). The wildfire emissions are obtained from the Fire INventory from NCAR (FINN), a widely used fire emission product in the

research community (37). The size distribution of primary particle emissions is assumed to observe lognormal distributions following the assumption of the default WRF-Chem (38). Since this study focuses on relatively pristine areas, especially the high altitudes where NPF dominates the particle concentration (*SI Appendix*, Fig. S2), the primary particle emissions have minimal effect on our simulation results.

3. Sources of observational data

We use a series of in-situ measurements over the Amazon basin to evaluate our model and support our main findings. Most measurements were achieved during the GoAmazon (Observations and Modelling of the Green Ocean Amazon) campaign (14, 39, 40) in both the wet and dry seasons of 2014 and the ACRIDICON–CHUVA (Aerosol, Cloud, Precipitation, and Radiation Interactions and Dynamics of Convective Cloud Systems – Cloud Processes of the Main Precipitation Systems in Brazil: A Contribution to Cloud Resolving Modeling and to the GPM) campaign (19, 41) in the dry season of 2014. Main pollution sources during the campaigns include anthropogenic emissions of Manaus (an isolated city of about two million people, see Fig. 1) from which the pollution plume generally follows the easterly or north-easterly trade winds during both seasons, and biomass burning emissions mainly in the southern part of the Amazon basin during the dry season. Our analysis focuses on measurements under relatively clean conditions to avoid the impact of these pollution sources. The G-1 aircraft was deployed during the GoAmazon campaign and was equipped with instruments for characterizing aerosol particles and trace gases. We use total aerosol number concentrations measured by a condensation particle counter (CPC, TSI model 3025, cutoff diameter 3 nm) and aerosol size distribution ranging from 10 nm to 400 nm in diameter characterized by a fast integrated mobility spectrometer (FIMS) at a time resolution of 1 Hz (40). Since the G-1 aircraft rarely flew for a sufficient time at different altitudes under pristine

conditions (its mission was mainly to sample the urban plumes downwind of Manaus) and it cannot fly above 6 km altitude, we also use total aerosol number concentration measurements from the HALO aircraft deployed in the ACRIDICON–CHUVA campaign. The measurements were done by a CPC (modified Grimm CPC 5.410 by Grimm Aerosol Technik) with a nominal cutoff diameter of 4 nm (19). However, due to inlet losses, the effective cutoff diameter increased to about 10 nm near the surface and about 20 nm at 150 hPa (about 13.8 km) (19). In addition, we employ continuous measurements of aerosol size distribution (from 10 nm to 430 nm in particle diameter) characterized by a scanning mobility particle sizer (SMPS, TSI model 3080) at the T0a (ATTO) site (9, 40), which is located to the upwind direction of Manaus and is thus under relatively pristine conditions during most of the simulation period (see Fig. 1). The measurements at T0a were made during the GoAmazon campaign and covered the entire simulation periods of this study.

Apart from aerosol number and size distribution measurements, we also compared our simulation results with observations of organic aerosol and sulfate mass concentrations, which have established connections to organic and inorganic NPF. The measurements were made with an Aerodyne High-Resolution Time-of-Flight Aerosol Mass Spectrometer (HR-ToF-AMS) onboard the G-1 aircraft during GoAmazon (14). We also evaluate the model against monoterpene concentrations measured by an Ionicon quadrupole high-sensitivity Proton-Transfer-Reaction Mass Spectrometer (PTR-MS) onboard G-1 (14).

4. Supplementary evaluation results of the model

In the main text, we have compared simulated aerosol number concentrations and size distributions at different heights with aircraft observations and showed a generally good agreement between our best-case scenario ("inorg+org_2D-VBS") and observational data. *SI Appendix*,

Fig. S12a illustrates the full time series of aerosol number concentration on March 7 from both G-1 measurements and model simulations. Consistent with Fig. 4a and Fig. 5, the results indicate that "nonuc" substantially underestimates observed aerosol number concentration at high altitudes while "inorg+org_2D-VBS" gets the magnitude of number concentration correct. Nevertheless, there are some discrepancies between the model results and observations in terms of the fluctuation of concentrations over time, indicating that the exact location and timing of NPF are more difficult to simulate probably because they depend on the complex interplay between chemistry and meteorology over very fine spatiotemporal scales.

SI Appendix, Fig. S12b,c further compares modeled time series of *organic aerosol (OA)* and *sulfate* mass concentrations with observations by a HR-ToF-AMS (see *SI Appendix*, Section 3). Considering that organics and H_2SO_4 are two major nucleating agents, the evaluation of OA and sulfate mass concentrations helps to check the reliability of the model results. The simulations generally agree with both the magnitude and variations of HR-ToF-AMS observations. For OA, observations show relatively high concentrations at low (< 3000 m) and high (> 5000 m) altitudes and relatively low concentrations at intermediate altitudes (3000–5000 m), which is reproduced by the model. For sulfate, both simulations and observations exhibit an obviously decreasing trend with increasing altitude, though the model slightly overestimates the sulfate concentrations near the surface.

We also evaluate simulated concentrations of *monoterpenes*, the precursors of ULVOC and ELVOC that drive organic NPF, against G-1 measurements (*SI Appendix*, Section 3) in the simulation periods during both wet and dry seasons. We find that the average simulated concentrations of 0.135 ppb and 0.125 ppb in the wet and dry seasons agree reasonably well with the corresponding observed values of 0.126 ppb and 0.104 ppb.

We then compare modelled aerosol number size distribution with surface observations that are available for a longer time period than aircraft measurements. We use observations at the T0a site, which is located to the upwind direction of Manaus and is thus under relatively pristine conditions during most of the simulation periods (see Fig. 1 for the site location and *SI Appendix*, Section 3 for a description of the observations). *SI Appendix*, Fig. S13a and b show the simulated and observed size distribution in the wet season and dry season, respectively. The model results agree with observations except for an underestimation of small particles, consistent with the evaluation results against G-1 measurements at the lowest altitude of 650 m on March 7 (Fig. 5a), probably because the rapid downward transport by convective downdrafts is not resolved by the 10 km grid spacing.

To investigate whether a higher model resolution could help to minimize the underestimation of small particles at low altitudes, we conducted a sensitivity simulation for March 7 using a finer grid spacing of 4 km. The modelled size distribution at 650 m is illustrated in *SI Appendix*, Fig. S14. No noticeable improvement is found in the 4 km simulation, implying that a higher resolution and even large eddy simulation (LES) might be needed to fully capture convective downdrafts, which warrants further in-depth studies.

5. Sensitivity analysis

Considering the uncertainty in organic-mediated NPF, we examine the impact of some key factors on simulated aerosol concentration and NPF mechanisms through sensitivity analysis. First, autoxidation is the most important formation mechanism of ULVOC and ELVOC and its rate is a strong function of temperature:

$$k = Aexp(-\theta_a/T)$$

where A is a pre-exponential factor, T is temperature, and θ_a is the energy barrier height, which governs the temperature dependence of the reaction rate. We use $\theta_a = 7500K$ in our base-case 2D-VBS. Praske et al. (42) summarized a number of studies and reported an uncertainty of 352 K in the barrier height. We design two sensitivity experiments ("high-barrier" and "low-barrier") by fixing the autoxidation rate at 298 K and varying the barrier height by ±500 K (+500 K for "high-barrier" and −500 K for "low-barrier") in a Clausius-Clapeyron-like expression. We fix the rate constant at 298 K because at that temperature we constrained the HOM yields against laboratory experiments and thus have more confidence in the reaction rate. Second, we use ULVOC/ELVOC with O:C > 0.4 to drive organic-mediated NPF in the base-case simulation. While the threshold of 0.4 has certain theoretical basis and indirect experimental support, it has not been rigorously established. Hence, we design another experiment ("O:C-all") in which we assume that ULVOC and ELVOC with all O:C values contribute to NPF. Finally, the strength of the temperature dependence of organic NPF rates is uncertain. In the base-case simulation, we apply a temperature dependence function which results in about a factor of 2.15 increase in NPF rate per 10 K of temperature decrease. To account for its uncertainty, we perform an sensitivity experiment with a stronger temperature dependence ("strong-T-dependence") in which we apply the function of Dunne et al. (43), i.e., $J_T = J_{278K}\exp(-(T-278)/10)$. Meanwhile, we conduct another experiment ("weak-T-dependence") which adopts a much weaker temperature dependence function of $J_T = J_{278K}\exp(-(T-278)/20)$, which translates into a factor of 1.6 increase in NPF rate per 10 K of temperature decrease. The results of these sensitivity analyses are summarized in *SI Appendix*, Figs. S4 and S5.

6. Vertical transport and its impact on aerosol concentrations

At a given altitude, aerosols originate not only from in-situ NPF, but also from vertical transport. *SI Appendix*, Fig. S6a,b illustrates the net vertical aerosol fluxes as a function of height over the relatively pristine area defined in the main text (red dashed rectangle in Fig. 1), simulated by our best-case scenario ("inorg+org_2D-VBS"). Particles smaller than 40 nm exhibit net downward fluxes at nearly all heights, indicating a continuous downward transport of small particles formed at high altitudes throughout the troposphere. Larger particles, however, show fluxes of different signs at different altitudes, suggesting that both the subsidence and growth of small new particles and the upward transport of boundary layer aerosols play significant roles. *SI Appendix*, Fig. S6c-f further examine statistically the impact of vertical transport on aerosol number concentrations at two representative vertical levels: 380 hPa (7.8 km), which is roughly the bottom of the upper troposphere, and 800 hPa (1.9 km), which is roughly the bottom of the free troposphere (top of boundary layer). As the vertical velocity changes from negative (descending) to positive (ascending) values, the particle number smaller than 40 nm decreases remarkably at both heights in both seasons, and the trends are all statistically significant at the 0.01 level based on Student's t-test, indicating that the downward transport effectively increases the concentrations of small particles at both heights. In contrast, particle number larger than 100 nm does not show an obvious trend with vertical velocity. As a combined effect, the total particle number concentration generally decreases when the vertical velocity changes from negative to positive, especially at 380 hPa, where small particles dominate the total particle number. We conclude from this analysis that the constant downward transport of an enormous number of newly formed particles in the upper troposphere acts as an important source of aerosol number concentrations across a wide range of altitudes, ranging from the lower part of the upper troposphere to the bottom of the free troposphere, under relatively pristine conditions. This extends

the findings of previous studies, which focused on how downward transport helps to sustain the aerosol number concentration at lower altitudes (primarily the boundary layer) of the tropics (40, 44).

7. Discussion of NPF mechanisms in tropical marine upper troposphere

While organic-mediated NPF has been shown to dominate in the Amazon upper troposphere, it remains uncertain whether similar mechanisms also play an important role in the tropical marine upper troposphere, where monoterpene concentrations are much lower. Correspondingly, some studies suggested that NPF in the marine tropical upper troposphere is mainly driven by sulfuric acid (45, 46). However, Williamson et al. (44) (Extended Data Fig. 7) showed that, in the upper troposphere of the tropical Atlantic, the sulfate mass concentration is very low but the organic mass concentration is elevated compared with middle altitudes. In that instance, organics probably dominate the composition of smaller particles, as indicated by the large difference between the organic concentrations obtained by AMS (measuring particles of 50–500 nm) and PALMS (particle analysis by laser mass spectrometry, measuring particles of 150–500 nm) at high altitudes. This indicates that organics play an important, if not dominant role in high-altitude particle growth, even in some marine environments. However, whether organics also make a considerable contribution to NPF in these environments remains an open question.

8. Sensitivity to isoprene emissions

McFiggans et al. (47) suggested that isoprene suppresses SOA formed from monoterpenes through two mechanisms, i.e., OH scavenging and product scavenging. The OH scavenging is inherently considered in the WRF-Chem model while the product scavenging is not. To examine the OH scavenging effect, we conduct a sensitivity run with isoprene emissions in the modeling domain turned off ("no isoprene" case). Compared with the "no isoprene" case, the inclusion of

isoprene in the base case reduces average surface OH concentrations over relatively clean areas (red dashed rectangle in Fig. 1, which is the focus area of this study) by 71–72% in both the wet-season and dry-season periods. As a result, the SOA concentrations formed from monoterpenes decrease by 15–16% in both simulation periods, consistent with the OH scavenging effect proposed by McFiggans et al. (47). Note that the monoterpene SOA only decreases slightly when OH decreases dramatically; this is also consistent with the simulation results by McFiggans et al. (47) using the EMEP MSC-W model and is explained by the fact that the decrease in SOA from the monoterpene + OH reaction is largely counteracted by the increase in SOA from the monoterpene + O_3 reaction (see Fig. 5 of McFiggans et al. (47)). Our current model does not distinguish monoterpene + OH SOA from monoterpene + O_3 SOA, which prevents us from analyzing the changes in these two components separately.

The current WRF-Chem does not consider the product scavenging effect, the inclusion of which is expected to further reduce simulated monoterpene SOA to some extent. The product scavenging should also suppress the NPF triggered by monoterpene oxidation products near the surface (48-50), because isoprene reduces the yield of highly-oxygenated dimers with about 20 carbon atoms that drive NPF, while increasing the production of dimers with about 15 carbon atoms (isoprene-monoterpene cross reaction products) (50). However, the impact on NPF in the upper troposphere may be more complicated, because dimers about 15 carbon atoms may also nucleate at low temperature due to reduced volatilities. Further studies are needed to systematically investigate the impact of isoprene on SOA and NPF, especially in the upper troposphere.

References

1. Schervish M, Donahue NM (2020) Peroxy radical chemistry and the volatility basis set. *Atmos. Chem. Phys.* 20(2):1183-1199.

2. Donahue NM, *et al.* (2012) Aging of biogenic secondary organic aerosol via gas-phase OH radical reactions. *P. Natl. Acad. Sci. USA.* 109(34):13503-13508.
3. Kirkby J, *et al.* (2016) Ion-induced nucleation of pure biogenic particles. *Nature* 533(7604):521-526.
4. Ehn M, *et al.* (2014) A large source of low-volatility secondary organic aerosol. *Nature* 506(7489):476-479.
5. Jokinen T, *et al.* (2015) Production of extremely low volatile organic compounds from biogenic emissions: Measured yields and atmospheric implications. *P. Natl. Acad. Sci. USA.* 112(23):7123-7128.
6. Sarnela N, *et al.* (2018) Measurement-model comparison of stabilized Criegee intermediate and highly oxygenated molecule production in the CLOUD chamber. *Atmos. Chem. Phys.* 18(4):2363-2380.
7. Berndt T, *et al.* (2016) Hydroxyl radical-induced formation of highly oxidized organic compounds. *Nat. Commun.* 7:13677.
8. Bela MM, *et al.* (2015) Ozone production and transport over the Amazon Basin during the dry-to-wet and wet-to-dry transition seasons. *Atmos. Chem. Phys.* 15(2):757-782.
9. Andreae MO, *et al.* (2015) The Amazon Tall Tower Observatory (ATTO): overview of pilot measurements on ecosystem ecology, meteorology, trace gases, and aerosols. *Atmos. Chem. Phys.* 15(18):10723-10776.
10. Shrivastava M, *et al.* (2019) Urban pollution greatly enhances formation of natural aerosols over the Amazon rainforest. *Nat. Commun.* 10:1046.
11. Liu Y, *et al.* (2016) Isoprene photochemistry over the Amazon rainforest. *P. Natl. Acad. Sci. USA.* 113(22):6125-6130.
12. Yanez-Serrano AM, *et al.* (2015) Diel and seasonal changes of biogenic volatile organic compounds within and above an Amazonian rainforest. *Atmos. Chem. Phys.* 15(6):3359-3378.
13. Jardine K, *et al.* (2011) Within-canopy sesquiterpene ozonolysis in Amazonia. *J. Geophys. Res-Atmos.* 116:D19301.
14. Shilling JE, *et al.* (2018) Aircraft observations of the chemical composition and aging of aerosol in the Manaus urban plume during GoAmazon 2014/5. *Atmos. Chem. Phys.* 18(14):10773-10797.
15. Bianchi F, *et al.* (2019) Highly oxygenated organic molecules (HOM) from gas-phase autoxidation involving peroxy radicals: a key contributor to atmospheric aerosol. *Chem. Rev.* 119(6):3472-3509.
16. Shilling JE, *et al.* (2008) Particle mass yield in secondary organic aerosol formed by the dark ozonolysis of alpha-pinene. *Atmos. Chem. Phys.* 8(7):2073-2088.
17. Presto AA, Donahue NM (2006) Investigation of alpha-pinene plus ozone secondary organic aerosol formation at low total aerosol mass. *Environ. Sci. Technol.* 40(11):3536-3543.
18. Ng NL, *et al.* (2007) Effect of NOx level on secondary organic aerosol (SOA) formation from the photooxidation of terpenes. *Atmos. Chem. Phys.* 7(19):5159-5174.
19. Andreae MO, *et al.* (2018) Aerosol characteristics and particle production in the upper troposphere over the Amazon Basin. *Atmos. Chem. Phys.* 18(2):921-961.
20. Shrivastava M, *et al.* (2011) Modeling organic aerosols in a megacity: comparison of simple and complex representations of the volatility basis set approach. *Atmos. Chem. Phys.* 11(13):6639-6662.

21. Stolzenburg D, *et al.* (2018) Rapid growth of organic aerosol nanoparticles over a wide tropospheric temperature range. *P. Natl. Acad. Sci. USA.* 115(37):9122-9127.
22. Carter WPL (2000) Documentation of the SAPRC-99 chemical mechanism for VOC reactivity assessment, Final report to California Air Resources Board Contract 92-329 and Contract 95-308. (University of California Riverside).
23. Zaveri RA, Easter RC, Fast JD, Peters LK (2008) Model for simulating aerosol interactions and chemistry (MOSAIC). *J. Geophys. Res-Atmos.* 113(D13):D13204.
24. Fahey KM, Pandis SN (2001) Optimizing model performance: variable size resolution in cloud chemistry modeling. *Atmos. Environ.* 35(26):4471-4478.
25. Hu ZY, *et al.* (2016) Trans-Pacific transport and evolution of aerosols: evaluation of quasi-global WRF-Chem simulation with multiple observations. *Geosci. Model. Dev.* 9(5):1725-1746.
26. Zhao C, *et al.* (2013) Uncertainty in modeling dust mass balance and radiative forcing from size parameterization. *Atmos. Chem. Phys.* 13(21):10733-10753.
27. Lawrence DM, *et al.* (2011) Parameterization Improvements and Functional and Structural Advances in Version 4 of the Community Land Model. *J. Adv. Model. Earth Syst.* 3:M03001.
28. Hong SY, Yign N, Dudhia J (2006) A new vertical diffusion package with an explicit treatment of entrainment processes. *Mon. Weather. Rev.* 134(9):2318-2341.
29. Grell GA, Freitas SR (2014) A scale and aerosol aware stochastic convective parameterization for weather and air quality modeling. *Atmos. Chem. Phys.* 14(10):5233-5250.
30. Morrison H, Thompson G, Tatarskii V (2009) Impact of cloud microphysics on the development of trailing stratiform precipitation in a simulated squall line: comparison of one- and two-moment schemes. *Mon. Weather. Rev.* 137(3):991-1007.
31. Clough SA, *et al.* (2005) Atmospheric radiative transfer modeling: a summary of the AER codes. *J. Quant. Spectrosc. Radiat. Transf.* 91(2):233-244.
32. Abdul-Razzak H, Ghan SJ (2002) A parameterization of aerosol activation. 3. Sectional representation. *J. Geophys. Res.* 107(D3):AAC1-1-6.
33. Easter RC, *et al.* (2004) MIRAGE: Model description and evaluation of aerosols and trace gases. *J. Geophys. Res-Atmos.* 109(D20):D20210.
34. Grell GA, Devenyi D (2002) A generalized approach to parameterizing convection combining ensemble and data assimilation techniques. *Geophys. Res. Lett.* 29(14):1693.
35. Guenther AB, *et al.* (2012) The Model of Emissions of Gases and Aerosols from Nature version 2.1 (MEGAN2.1): an extended and updated framework for modeling biogenic emissions. *Geosci. Model. Dev.* 5(6):1471-1492.
36. Zhao C, *et al.* (2016) Sensitivity of biogenic volatile organic compounds to land surface parameterizations and vegetation distributions in California. *Geosci. Model. Dev.* 9(5):1959-1976.
37. Wiedinmyer C, *et al.* (2011) The Fire INventory from NCAR (FINN): a high resolution global model to estimate the emissions from open burning. *Geosci. Model. Dev.* 4(3):625-641.
38. Lupascu A, *et al.* (2015) Modeling particle nucleation and growth over northern California during the 2010 CARES campaign. *Atmos. Chem. Phys.* 15(21):12283-12313.

39. Martin ST, *et al.* (2017) The Green Ocean Amazon experiment (GoAmazon2014/5) observes pollution affecting gases, aerosols, clouds, and rainfall over the rain forest. *B. Am. Meteorol. Soc.* 98(5):981-997.
40. Wang J, *et al.* (2016) Amazon boundary layer aerosol concentration sustained by vertical transport during rainfall. *Nature* 539(7629):416-419.
41. Wendisch M, *et al.* (2016) ACRIDICON-CHUVA campaign: studying tropical deep convective clouds and precipitation over Amazonia using the new German research aircraft HALO. *B. Am. Meteorol. Soc.* 97(10):1885-1908.
42. Praske E, *et al.* (2018) Atmospheric autoxidation is increasingly important in urban and suburban North America. *P. Natl. Acad. Sci. USA.* 115(1):64-69.
43. Dunne EM, *et al.* (2016) Global atmospheric particle formation from CERN CLOUD measurements. *Science* 354(6316):1119-1124.
44. Williamson CJ, *et al.* (2019) A large source of cloud condensation nuclei from new particle formation in the tropics. *Nature* 574(7778):399-403.
45. Clarke AD, *et al.* (1999) Nucleation in the equatorial free troposphere: Favorable environments during PEM-Tropics. *J. Geophys. Res-Atmos.* 104(D5):5735-5744.
46. Clarke AD, Kapustin VN (2002) A pacific aerosol survey. Part I: A decade of data on particle production, transport, evolution, and mixing in the troposphere. *J. Atmos. Sci.* 59(3):363-382.
47. McFiggans G, *et al.* (2019) Secondary organic aerosol reduced by mixture of atmospheric vapours. *Nature* 565(7741):587-593.
48. Kiendler-Scharr A, *et al.* (2009) New particle formation in forests inhibited by isoprene emissions. *Nature* 461(7262):381-384.
49. Lee SH, *et al.* (2016) Isoprene suppression of new particle formation: Potential mechanisms and implications. *J. Geophys. Res-Atmos.* 121(24):14621-14635.
50. Heinritzi M, Dada L, Simon M, Stolzenburg D, Wagner AC (2020) Molecular understanding of the suppression of new-particle formation by isoprene. *Atmos. Chem. Phys. Discuss.*:10.5194/acp-2020-5151.

Figures and Tables

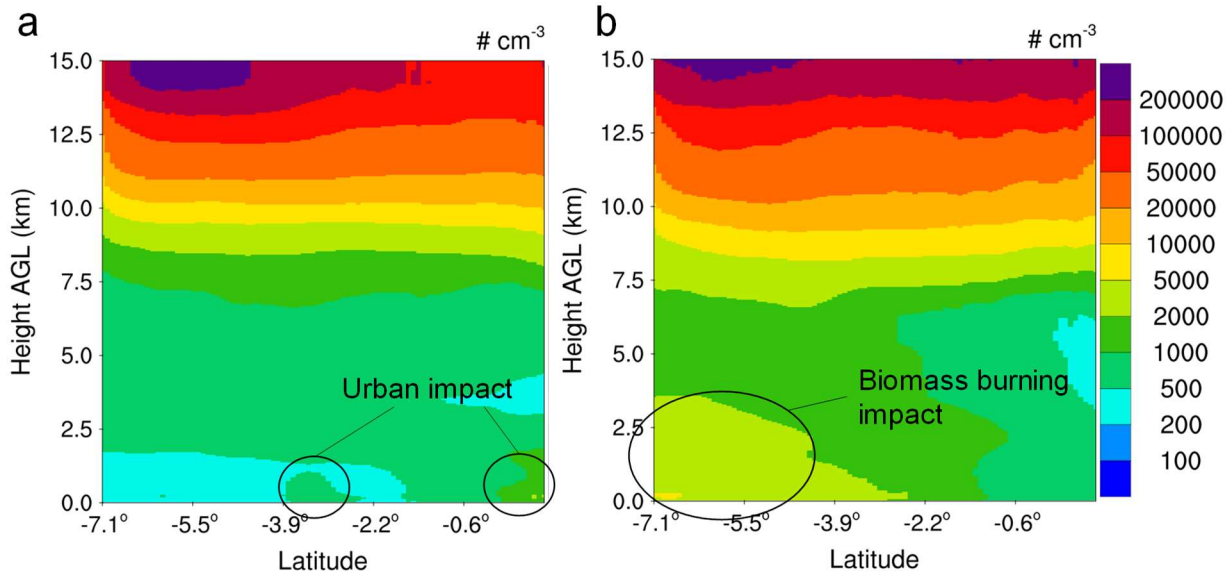

Figure S1. Zonal mean number concentration of aerosols larger than 3 nm diameter in the modeling domain averaged during the (a) wet season and (b) dry season periods, simulated by the "inorg+org_2D-VBS" scenario. The aerosol number concentrations are normalized to standard temperature and pressure (STP; 273.15 K and 101.325 kPa). The results show that the high aerosol concentration in the upper troposphere is ubiquitous, regardless of whether it is close to the urban or biomass-burning areas.

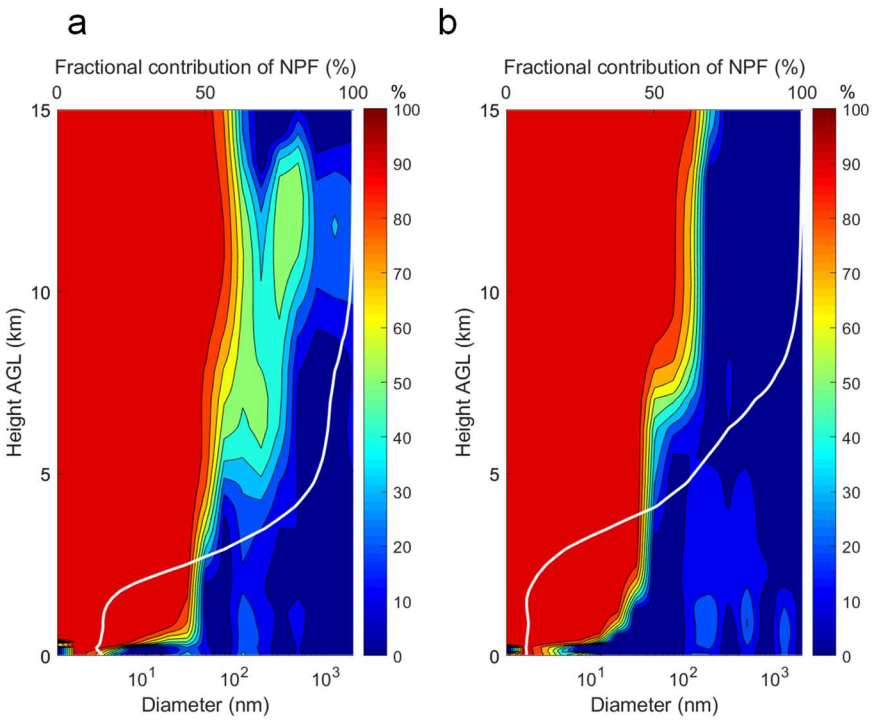

Figure S2. Averaged fractional contribution to aerosol number concentration of NPF occurring within the modeling domain as a function of height during the (a) wet season and (b) dry season periods. The white line represents the fractional contribution to total aerosol number concentration and the contours represent the contributions to size-resolved aerosol number concentrations. The contribution is quantified using the difference between the "inorg+org_2D-VBS" and "nonuc" scenarios. Note that this figure does not account for the contribution of NPF occurring outside of the modeling domain, which may contribute a large fraction of the particle number at low altitudes.

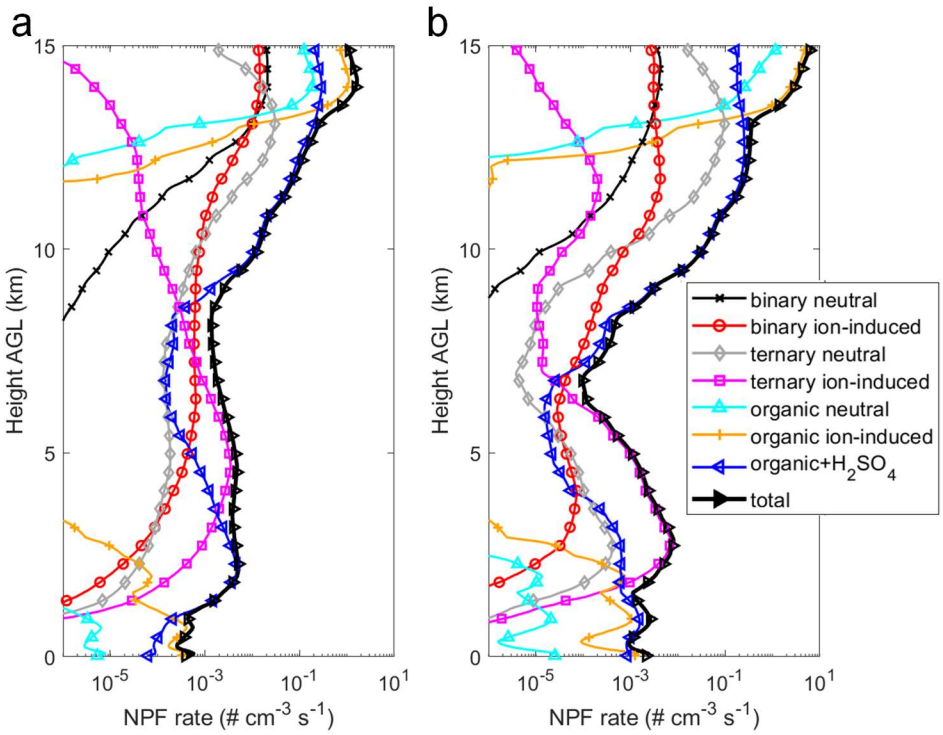

565

566 **Figure S3**. NPF rates from seven pathways and the total NPF rate at a diameter of 1.7 nm ($J_{1.7}$) averaged
567 over relatively clean areas (red dashed rectangle in Fig. 1) during the (a) wet season and (b) dry season
568 periods, simulated by the "inorg+org_2D-VBS" scenario.

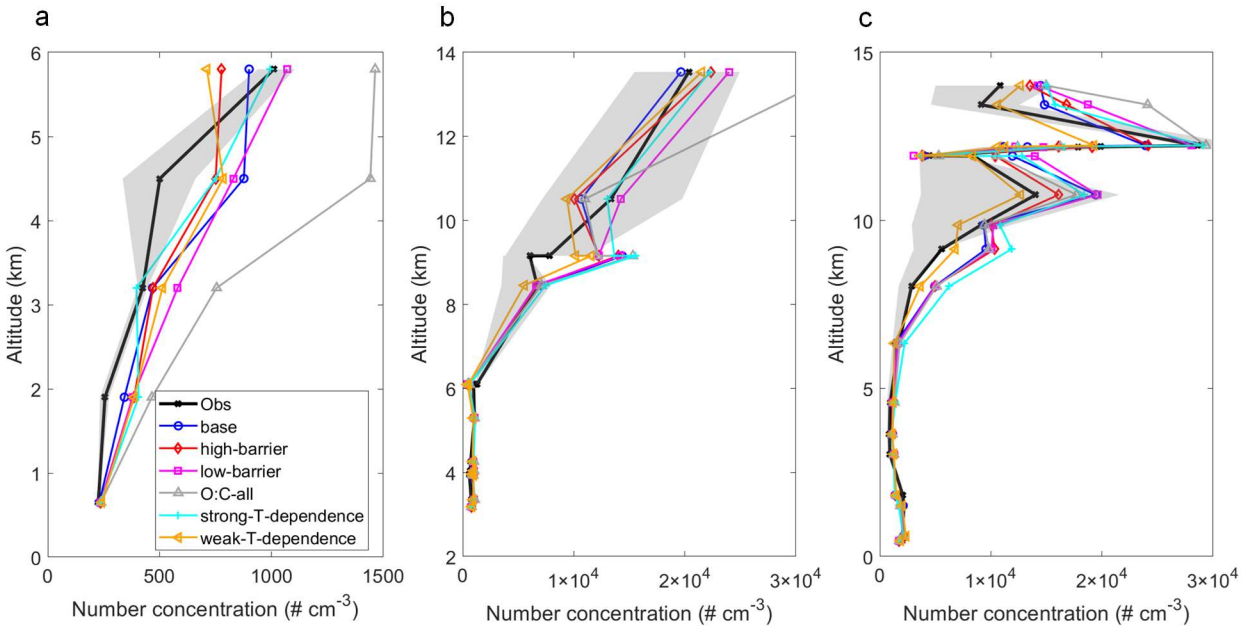

Figure S4. The same as Fig. 4 but for the base case (i.e., "inorg+org_2D-VBS") and different sensitivity simulations. The lines are mean concentrations within each vertical bin while the shaded areas represent the 25th to 75th percentiles of the observations. The definitions of the sensitivity scenarios are described in *SI Appendix*, Section 5 and Table S1.

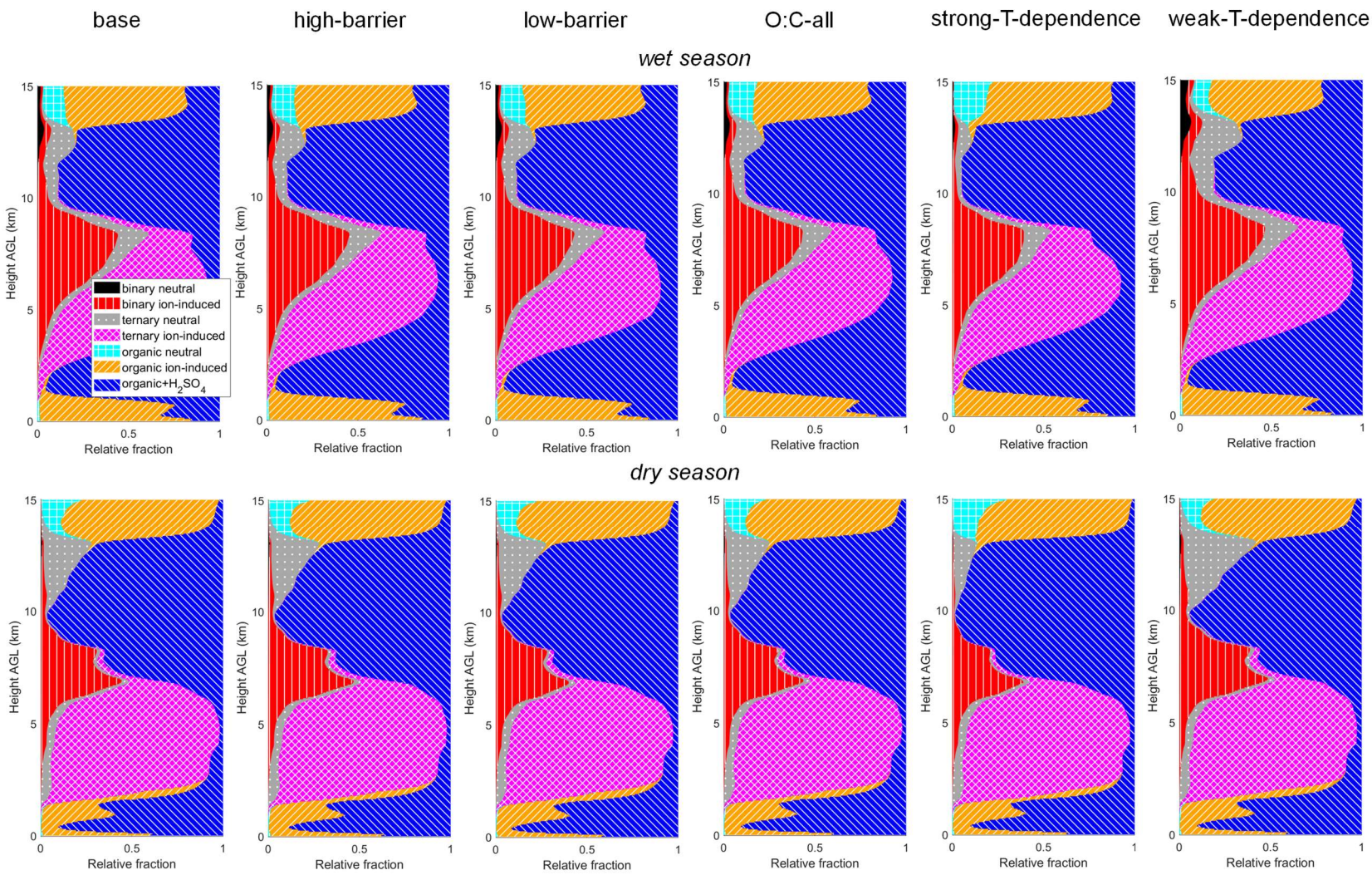

Figure S5. Relative contributions of seven different NPF mechanisms averaged over relatively clean areas (red dashed rectangle in Fig. 1) for the base case (i.e., "inorg+org_2D-VBS") and different sensitivity simulations. The definitions of the sensitivity scenarios are described in *SI Appendix*, Section 5 and Table S1.

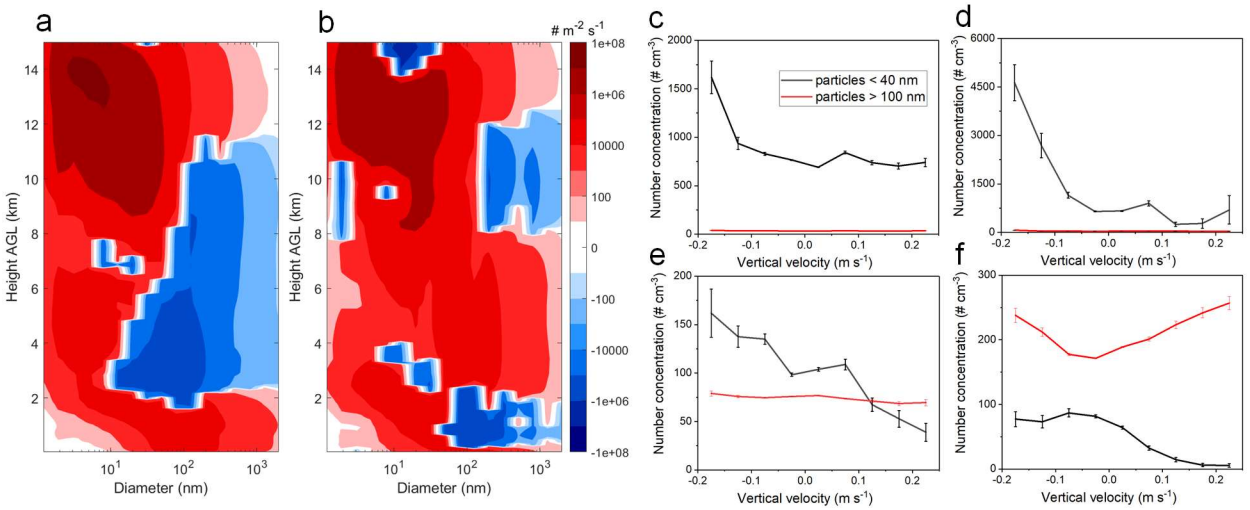

578

579 **Figure S6.** Vertical transport of aerosols and its contribution to aerosol number concentrations, simulated
580 by the "inorg+org_2D-VBS" scenario. (a, b) Net vertical aerosol fluxes as a function of height, averaged
581 over relatively clean areas (red dashed rectangle in Fig. 1) during the (a) wet season and (b) dry season
582 periods. Positive and negative fluxes represent downward and upward transport, respectively. (c-f)
583 Variations in the number concentrations of small (D_p < 40 nm) and large particles (D_p > 100 nm) with
584 vertical velocity at (c, d) 380 hPa (7.8 km) and (e, f) 800 hPa (1.9 km) during the (c, e) wet season and (d,
585 f) dry season periods. Positive and negative vertical velocities represent ascending and descending motions,
586 respectively. The error bars are standard error of the mean ($\sigma/\sqrt{N}$), where N is the sample number (i.e., the
587 number of grid points falling within each bin of vertical velocity) and σ is the standard deviation. The
588 aerosol number concentrations are normalized to STP.

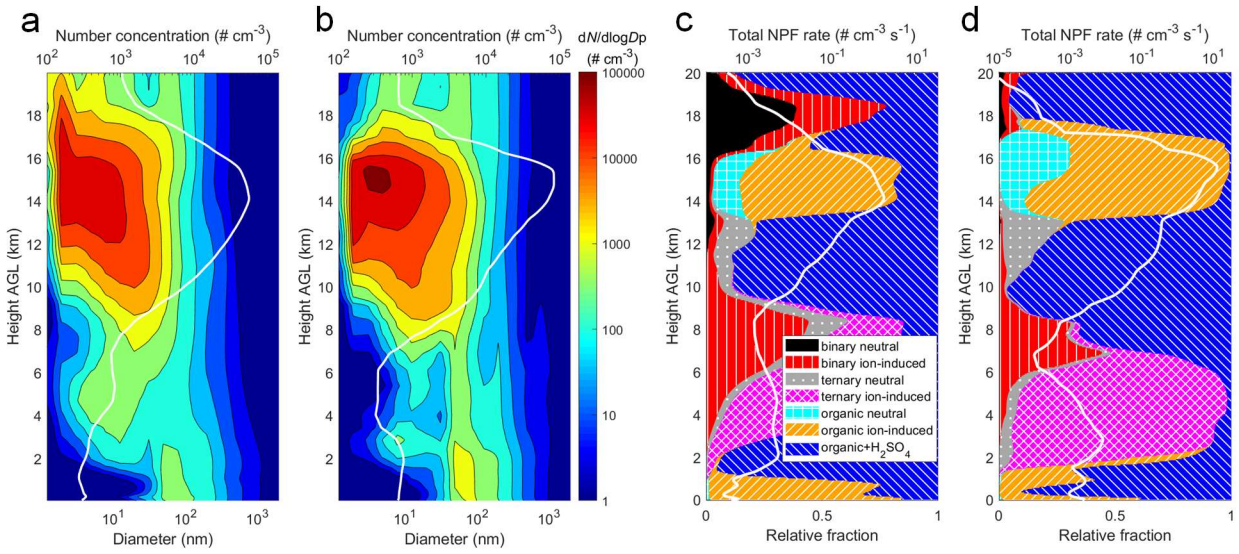

Figure S7. The same as Fig. 2 in the main text except that the height range is extended from 0–15 km to 0–20 km. The aerosol number concentration, total NPF rate, and organic NPF rates decrease dramatically with increasing height near the tropopause (16–18 km), mainly because the concentrations of organics decrease substantially with height at these altitudes (see *SI Appendix*, Fig. S8).

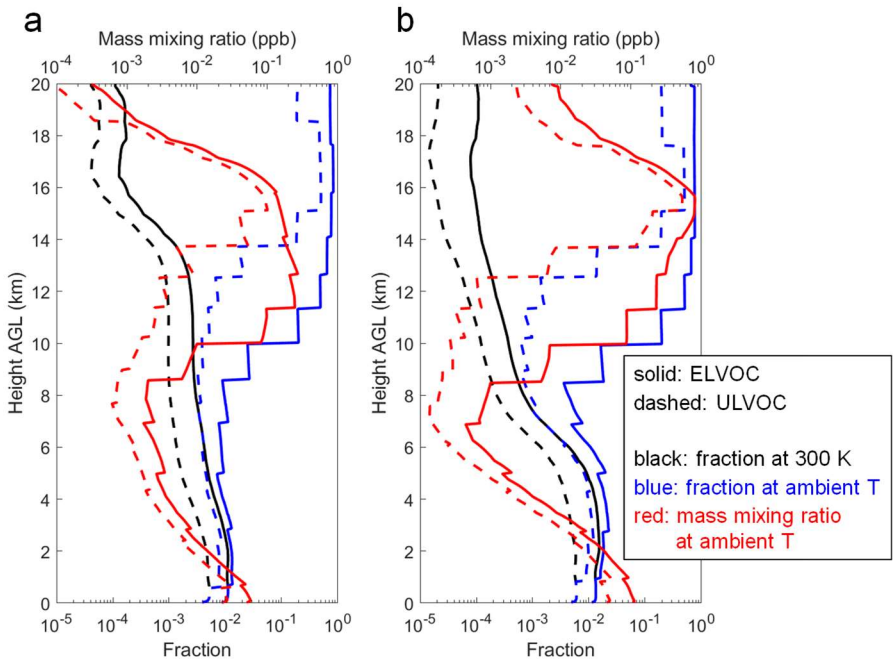

Figure S8. The same as Fig. 3 in the main text except that the height range is extended from 0–15 km to 0–20 km. The mixing ratios of ULVOC and ELVOC decrease dramatically with increasing height near the tropopause (16–18 km), mainly because their precursors (monoterpenes) are difficult to be lifted to these altitudes due to weakened vertical mixing near the tropopause.

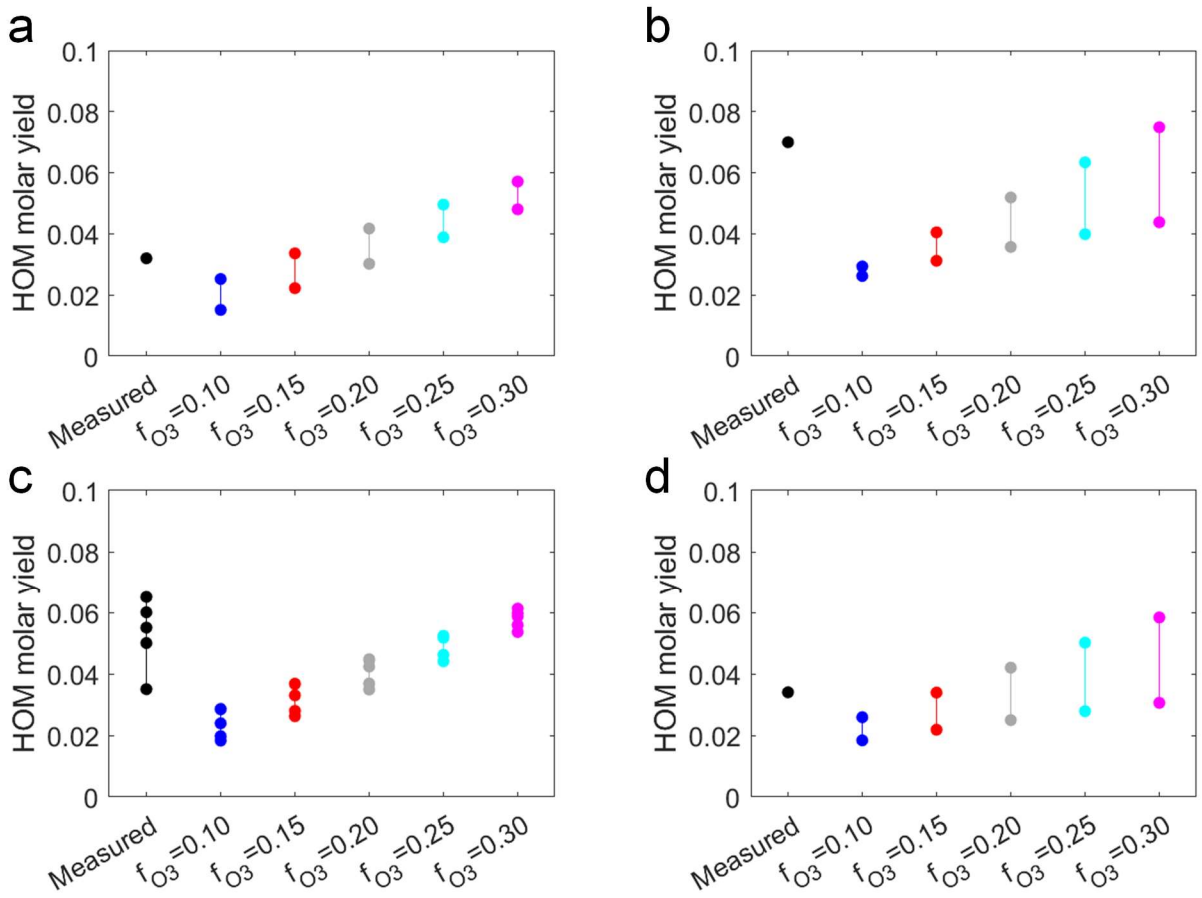

Figure S9. Comparison of 2D-VBS simulated HOM molar yields with laboratory experiments on α-pinene + O_3, using different fractions of first-generation peroxy radicals that can potentially autoxidize (f_{O3}). Panels (a–d) show comparison results with measurements from Kirkby et al. (3), Ehn et al. (4), Sarnela et al. (6), and Jokinen et al. (5), respectively. Each colored dot represents the measured HOM yield for an experiment or the simulated HOM yield for a model run. In (a, b, d) we only show one dot for measurements because the corresponding literature only reports the mean HOM yield for all experiments.

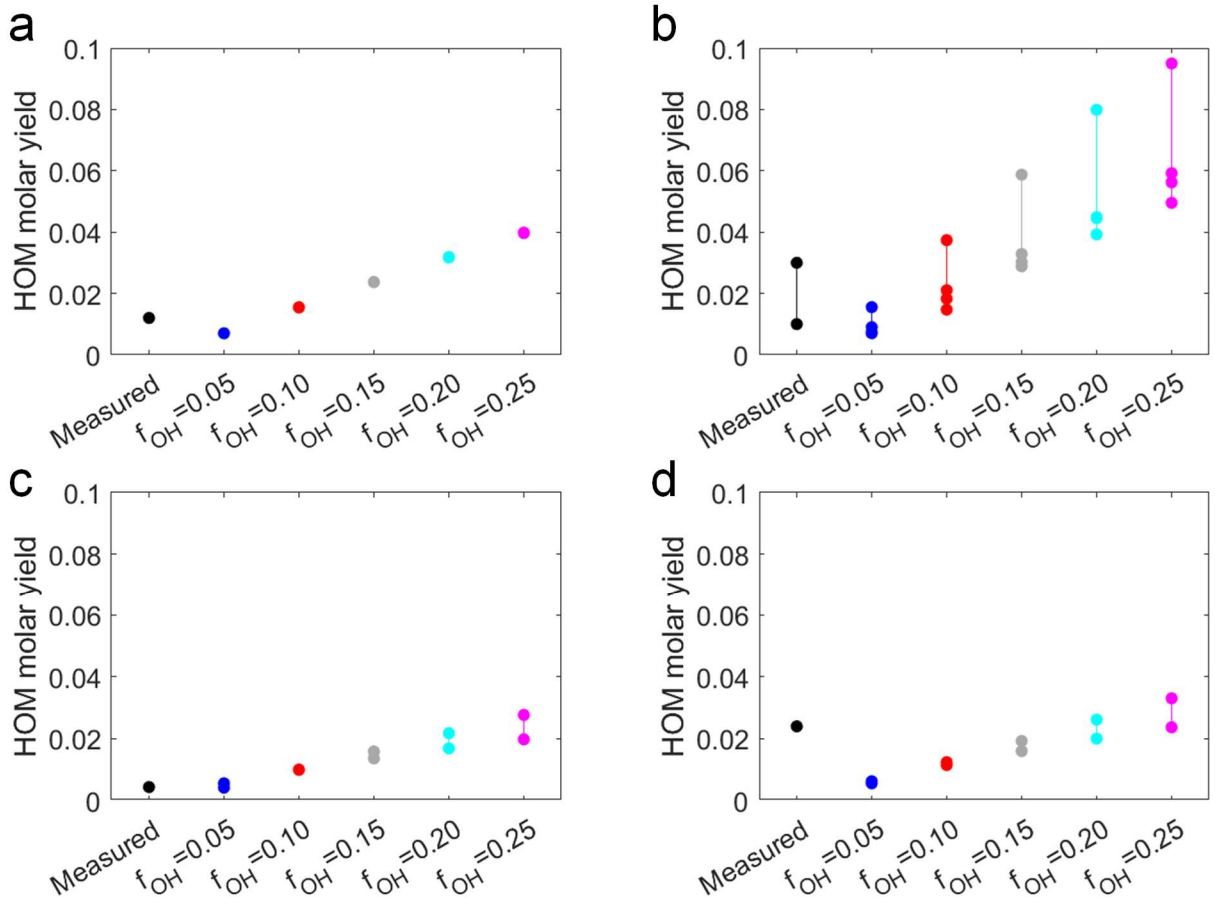

Figure S10. Comparison of 2D-VBS simulated HOM molar yields with laboratory experiments on α-pinene + OH, using different fractions of first-generation peroxy radicals that can potentially autoxidize (f_{OH}). Panels (a–d) show comparison results with measurements from Kirkby et al. (3), Ehn et al. (4), Jokinen et al. (5), and Berndt et al. (7), respectively. The meaning of colored dots is the same as that of Fig. S9.

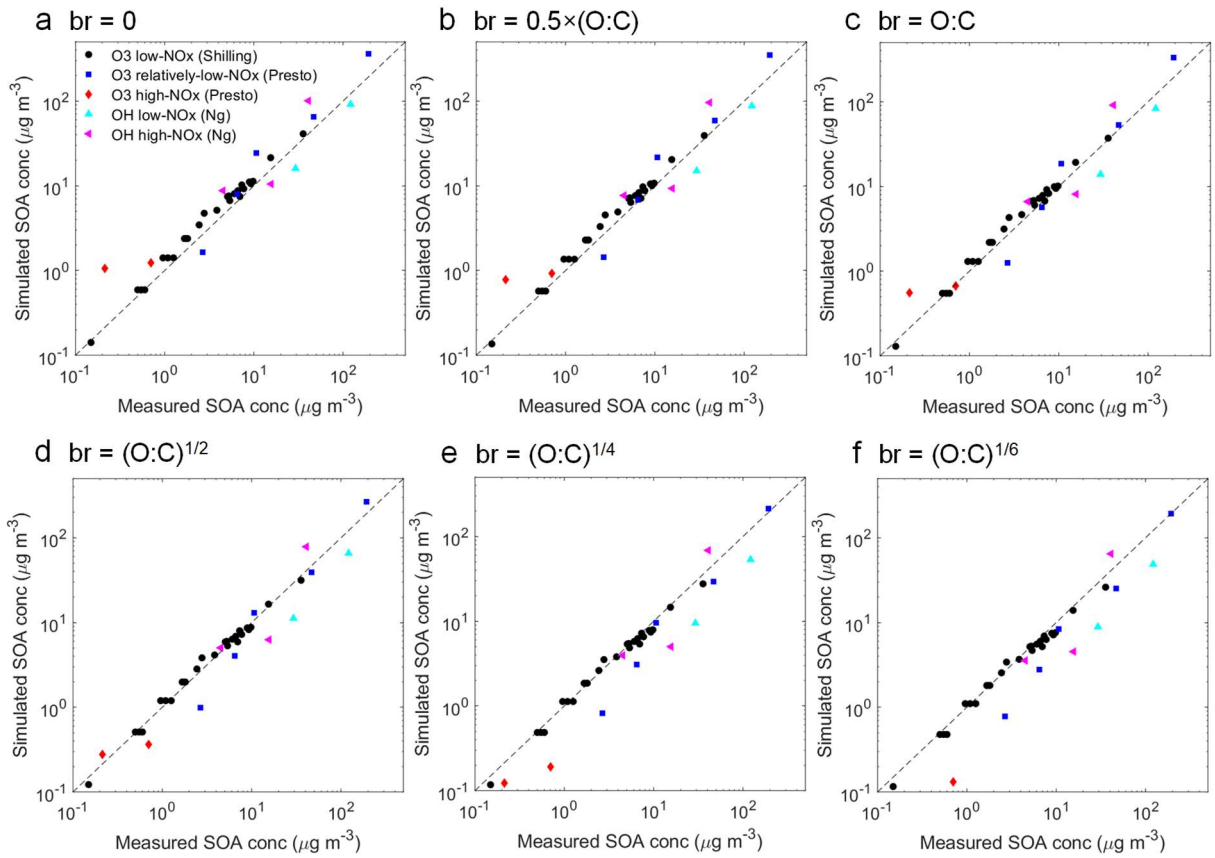

Figure S11. Model-measurement comparison of SOA concentrations for 2D-VBS simulations using different *br* vs. laboratory experiments involving reactions of α-pinene with O_3 and OH, under both high-NO_x and low-NO_x conditions. Panel (a–f) show comparison results with different parameterizations of *br*, where the *br* at a certain O:C gradually increases from (a) to (f). The experimental conditions are summarized in Table 1 of Shilling et al. (16), Table 1 of Presto et al. (17), and Table 2 of Ng et al. (18).

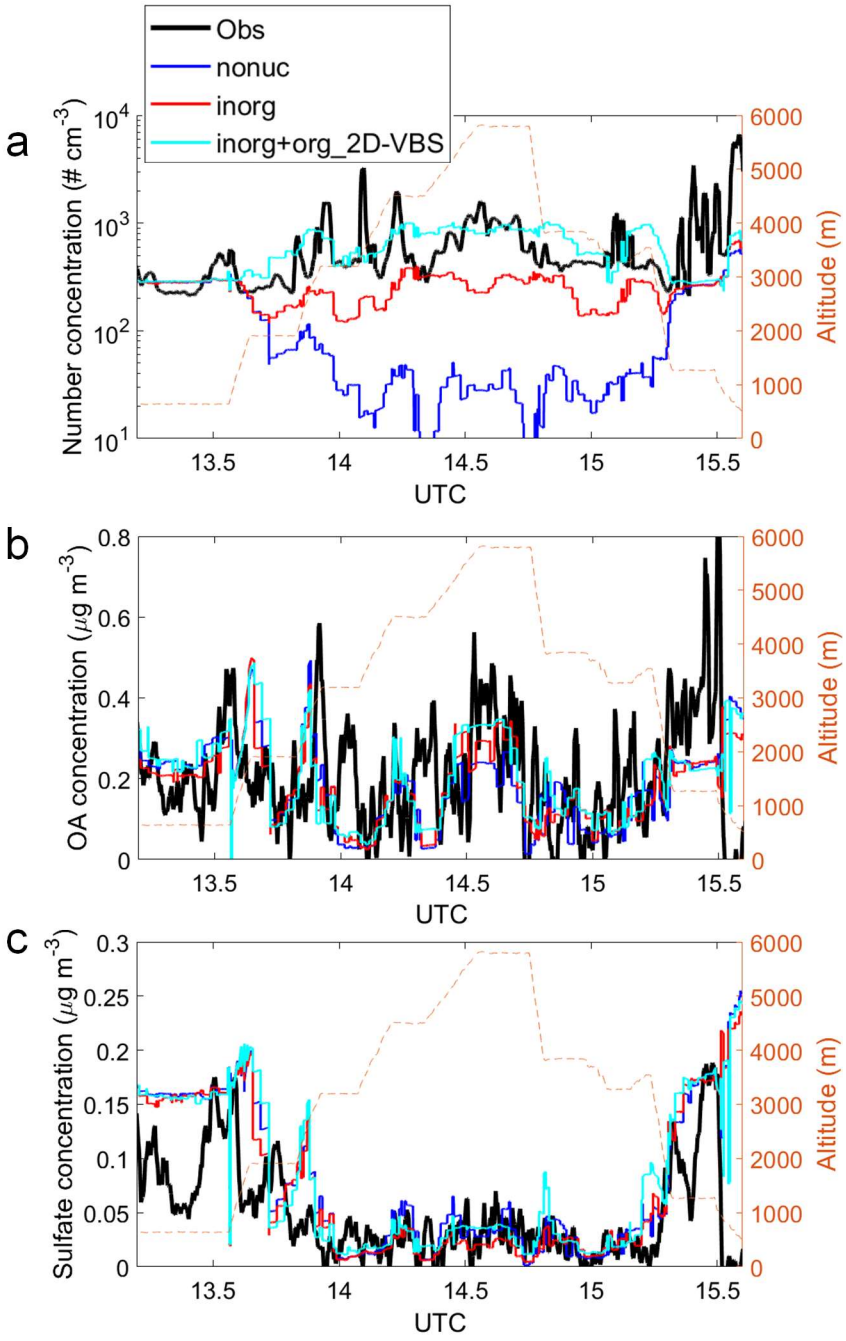

Figure S12. Comparison of simulated aerosol concentration with G-1 aircraft measurements on March 7. (a) aerosol number concentration, (b) organic aerosol (OA) mass concentration, and (c) sulfate mass concentration. The orange dashed line represents the aircraft altitude (right axis). The aerosol number and mass concentrations are normalized to STP. The definitions of the model scenarios are provided in the main text and in *SI Appendix*, Table S1. Details of the observational data are described in *SI Appendix*, Section 3.

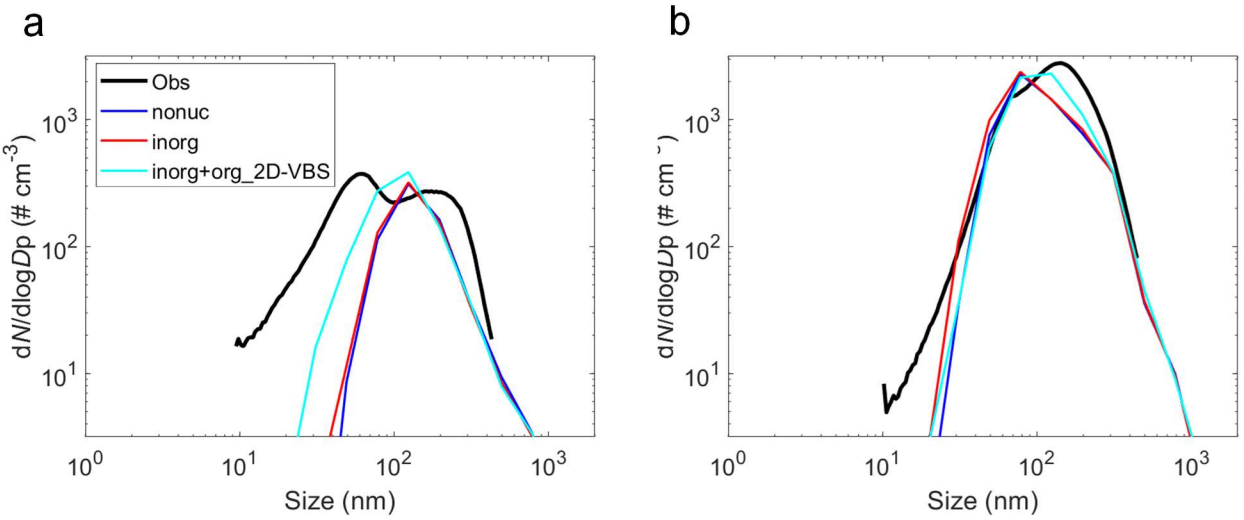

Figure S13. Comparison of simulated aerosol number size distribution with surface observation at the T0a site during the (a) wet season and (b) dry season periods. The aerosol size distributions are normalized to STP. The definitions of the model scenarios are provided in the main text and in *SI Appendix*, Table S1. Details of the observational data are described in *SI Appendix*, Section 3.

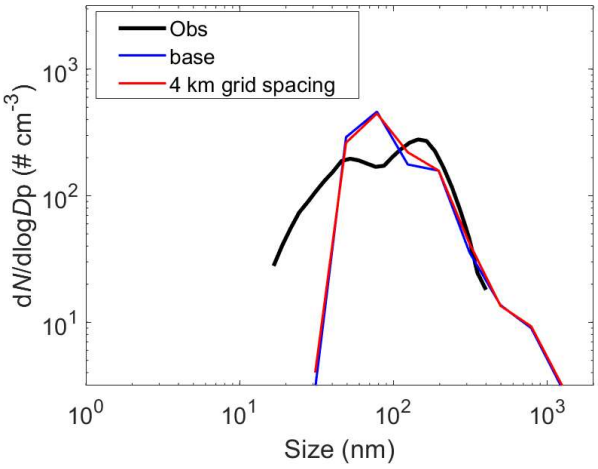

Figure S14. Comparison of aerosol number size distribution simulated by 4 km grid spacing with G-1 measurements at 650 m altitude on March 7. Details of the observational data are described in *SI Appendix*, Section 3.

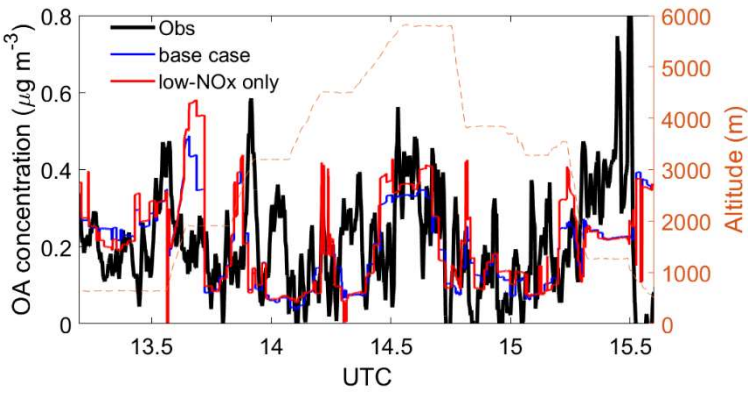

633

634 **Figure S15.** Comparison of simulated OA concentrations with G-1 aircraft measurements on March 7. The
635 "low-NO_x only" case is the same as the base case except that the 2D-VBS parameters are determined only
636 based on evaluation against low-NO_x experiments. The orange dashed line represents the aircraft altitude
637 (right axis). The OA concentrations are normalized to STP (273.15 K and 101.325 kPa). The definitions of
638 the model scenarios are provided in the text and in SI Appendix, Table S1.

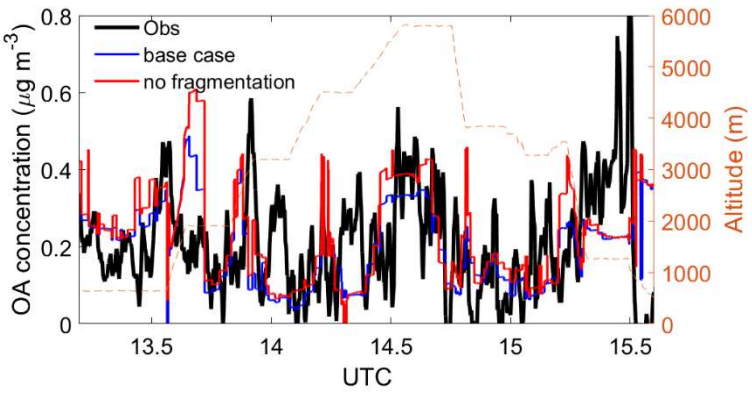

Figure S16. Comparison of simulated OA concentrations with G-1 aircraft measurements on March 7. The "no fragmentation" case is the same as the base case except that fragmentation is not assumed to occur, which is the default assumption of Schervish and Donahue (1). The orange dashed line represents the aircraft altitude (right axis). The OA concentrations are normalized to STP. The definitions of the model scenarios are provided in the text and in SI Appendix, Table S1.

Table S1. Summary of model scenarios developed in this study.

Scenario	Description
Main scenarios	
nonuc	A simulation without NPF.
inorg	A simulation with only inorganic NPF included.
inorg+org_simple	A simulation with both inorganic and organic NPF included, and the organics that nucleate are assumed to be a fixed fraction of all monoterpene oxidation products.
inorg+org_2D-VBS	A simulation with both inorganic and organic NPF included, and the organics that nucleate are simulated using the radical 2D-VBS framework. This is considered as the best-case scenario and used in most analyses of the present study. It is also used as the "base case" for sensitivity scenarios below.
Sensitivity scenarios	
high-barrier	Based on "inorg+org_2D-VBS", this scenario fixes autoxidation rate at 298 K and increases the barrier height by 500 K in a Clausius-Clapeyron-like expression. This results in a stronger temperature dependence of autoxidation rate.
low-barrier	Based on "inorg+org_2D-VBS", this scenario fixes autoxidation rate at 298 K and decreases the barrier height by 500 K in a Clausius-Clapeyron-like expression. This results in a weaker temperature dependence of autoxidation rate.
O:C-all	The same as "inorg+org_2D-VBS" except that ULVOC and ELVOC with all O:C values are assumed to drive pure-organic and organic+H_2SO_4 NPF, respectively.
strong-T-dependence	The same as "inorg+org_2D-VBS" except that a stronger temperature dependence function of NPF rate is used for organic-mediated NPF.
weak-T-dependence	The same as "inorg+org_2D-VBS" except that a weaker temperature dependence function of NPF rate is used for organic-mediated NPF.
4 km grid spacing	The same as "inorg+org_2D-VBS" except that a 4 km grid spacing is used instead of 10 km.
low-NO_x only	The same as "inorg+org_2D-VBS" except that the 2D-VBS parameters are determined only based on evaluation against low-NO_x experiments.
no fragmentation	The same as "inorg+org_2D-VBS" except that fragmentation is not assumed to occur, which is the default assumption of Schervish and Donahue (1).
no isoprene	The same as "inorg+org_2D-VBS" except that isoprene emissions in the modeling domain are turned off.

Table S2. Summary of the reaction conditions for laboratory experiments that measure HOM yields from α-pinene + O_3 reaction and the corresponding conditions for 2D-VBS simulations.

		Experimental conditions	Conditions for 2D-VBS simulations [a]				
			Run 1	Run 2	Run 3	Run 4	Run 5
Kirkby et al. (3)	α-pinene conc (ppb)	0.07–0.44 (~10 expts)	0.07	0.44			
	O_3 conc (ppb)	21–35 (~10 expts)	28	28			
	OH conc (mole cm^{-3})	--	--	--			
	T (K)	278	278	278			
Ehn et al. (4)	α-pinene conc (ppb)	0–30 (> 50 expts)	0.5	15			
	O_3 conc (ppb)	12–86 (> 50 expts)	40	40			
	OH conc (mole cm^{-3})	--	--	--			
	T (K)	289	289	289			
Sarnela et al. (6)	α-pinene conc (ppb)	0.08–0.6 (5 expts)	0.08	0.08	0.6	0.17	0.53
	O_3 conc (ppb)	22–24 (5 expts)	22	24	22	22	22
	OH conc (mole cm^{-3})	--	--	--	--	--	--
	T (K)	278	278	278	278	278	278
Jokinen et al. (5)	α-pinene conc (ppb)	0.085–160 (~10 expts)	0.2	50			
	O_3 conc (ppb)	21.9–23.3 (~10 expts)	23	23			
	OH conc (mole cm^{-3})	--	--	--			
	T (K)	293	293	293			

[a] For all simulations, $br = (O{:}\,C)^{1/2}$ and f_{OH} = 0.10; f_{O3} ranges from 0.10 to 0.30 (see Fig. S9).

Table S3. The same as Table S2 but for α-pinene + OH reaction.

		Experimental conditions	Conditions for 2D-VBS simulations [a]			
			Run 1	Run 2	Run 3	Run 4
Kirkby et al. (3)	α-pinene conc (ppb)	0.84–0.91 (~12 expts)	0.875	0.875		
	O_3 conc (ppb)	--	--	--		
	OH conc (mole cm^{-3})	$(0.4–2)\times10^5$ (~12 expts)	4×10^4	2×10^5		
	T (K)	278	278	278		
Ehn et al. (4)	α-pinene conc (ppb)	0.1–17 (> 30 expts)	0.5	0.5	10	10
	O_3 conc (ppb)	--	--	--	--	--
	OH conc (mole cm^{-3})	8×10^6 to 4×10^8 (> 30 expts)	1×10^7	1×10^8	1×10^7	1×10^8
	T (K)	289	289	289	289	289
Jokinen et al. (5)	α-pinene conc (ppb)	0.085–160 (~10 expts)	0.2	50		
	O_3 conc (ppb) [b]	21.9–23.3 (~10 expts)	23	23		
	OH conc (mole cm^{-3}) [b]	--	--	--		
	T (K)	293	293	293		
Berndt et al. (7)	α-pinene conc (ppb)	0.44–93 (> 40 expts)	1.0	40		
	O_3 conc (ppb) [b]	23 (> 40 expts)	23	23		
	OH conc (mole cm^{-3}) [b]	--	--	--		
	T (K)	295	295	295		

[a] For all simulations, $br = (O{:}\ C)^{1/2}$ and f_{O3} = 0.25; f_{OH} ranges from 0.05 to 0.25 (see Fig. S10).

[b] For the experiments conducted by Jokinen et al. (5) and Berndt et al. (7), OH is generated by α-pinene + O_3 reaction rather than being directly added to the system.